

Non-Reciprocal Interactions Reshape Topological Defect Annihilation

Ylann Rouzairé,^{1,2,*} Demian Levis,^{1,2} and Ignacio Pagonabarraga^{1,2}

¹*Departament de Física de la Materia Condensada,*

Universitat de Barcelona, Martí i Franquès 1, E08028 Barcelona, Spain

²*UBICS University of Barcelona Institute of Complex Systems, Martí i Franquès 1, E08028 Barcelona, Spain*

(Dated: January 24, 2024)

We show how non-reciprocal ferromagnetic interactions between neighbouring planar spins in two dimensions, affects the behaviour of topological defects. Non-reciprocity is introduced by weighting the coupling strength of the two-dimensional XY model by an anisotropic kernel. As a consequence, in addition to the topological charge q , the actual shape (or phase) of the defects becomes crucial to faithfully describe their dynamics. Non-reciprocal coupling twists the spin field, selecting specific defect shapes, dramatically altering the pair annihilation process. Defect annihilation can either be enhanced or hindered, depending on the shape of the defects concerned and the degree of non-reciprocity in the system.

Collective excitations in the form of topological defects are known to control the large-scale behaviour of a broad class of equilibrium systems, and to be eventually responsible for a Kosterlitz-Thouless (KT) phase transition, as exhibited by the two-dimensional ($2d$) XY model [1–3]. Being local singularities of the relevant order parameter field, topological defects can be considered as quasi-particles (characterised by their charge q), robust against perturbations [4–6], and the study of their dynamics provides insights into the ordering mechanisms at play [7–11]. Out-of-equilibrium, topological defects exhibit distinctive dynamical features, such as self-propulsion or super-diffusion, often breaking the symmetry between oppositely charged defects [12–20]. In active systems, for which their elementary constituents can self-generate stresses, the dynamics of defects has been recently identified with a growing number of biological processes [21–24]. Although the impact of defects on the critical properties of active matter is still to be settled [25–28], understanding their dynamics can clarify self-organisation mechanisms in living systems and eventually inspire the design of novel materials.

Non-reciprocal interactions provide an alternative route to conceive systems locally driven out-of-equilibrium. Indeed, the effective interactions between non-equilibrium agents generically violates the *actio-reactio* principle. Examples include microorganisms [29], social agents [30–34], catalytic colloids [35] or specifically tailored robot swarms [36–38]. The analysis of both particle and spin models, and continuum theories, have recently shown that non-reciprocal interactions give rise to spontaneous currents, patterns and non-equilibrium phase transitions [20, 37, 39–49].

To decipher the impact of non-reciprocity on the behaviour of topological defects, we consider an extension of the $2d$ XY model where a given spin interacts with its neighbourhood in a way that depends on the state of the spin itself: interactions are stronger along the spins' heading direction. We spell out the profound impact that such non-reciprocity has on the defects dynamics. In the

present case, not just the charge but the actual shape of a topological defect, superfluous in equilibrium, plays a key role. Non-reciprocity twists the spin field around defects, resulting in a complex annihilation kinetics.

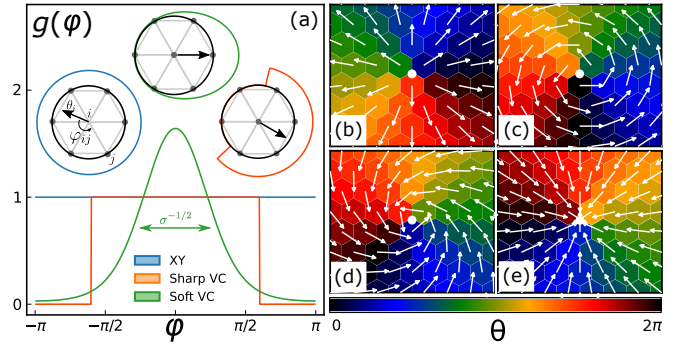


FIG. 1. **(a)** Sketch of the nearest neighbours coupling: the isotropic reciprocal case, in blue, the sharp vision cone, in orange, and our smooth version, in green (using $\sigma = 5$). **(b-e)** Four different $+1$ defects with (b) $\mu_+ = 0$, (c) $\mu_+ = \pi/2$, (d) $\mu_+ = 3\pi/4$, (e) $\mu_+ = \pi$. Spins sit on a triangular lattice (coordination 6). The white dot shows the defect core, on the dual (hexagonal) lattice. The cyclic colour code displays the phase θ of each spin.

Our system is composed of spins $\mathbf{S}_i = (\cos \theta_i, \sin \theta_i)$ sitting on the nodes of a triangular lattice of linear size L , and evolving accordingly to

$$\gamma \dot{\theta}_i = J \sum_{j \in \partial_i} g_\sigma(\varphi_{ij}) \sin(\theta_j - \theta_i) + \sqrt{2\gamma T} \eta_i(t) \quad (1)$$

where γ is the damping coefficient, J the coupling, η a Gaussian white noise with zero mean and unit variance and T the temperature of the bath to which the system is coupled (fixing $k_B = 1$). Non-reciprocal (NR) interactions are introduced by weighting the coupling between two neighbouring spins, say i and j , according to the orientation of spin i with respect to the direction of the bond connecting the two, denoted φ_{ij} (see sketch Fig.1(a)). This is encoded in the kernel g_σ : the

reciprocal $2dXY$ model with overdamped (non-conserved) dynamics [9] is recovered for constant g_σ , while “vision cone” interactions would correspond to a step function kernel [31, 48, 50]. We consider instead a “smooth vision cone”, based on the Von Mises distribution: $g_\sigma(\varphi) = \exp(\sigma \cos \varphi)$ [51]. Such function avoids several discretisation effects (discussed in the SM [52]) and allows considering other ways of breaking the action-reaction principle. As in the small φ regime $g_\sigma(\varphi) \sim e^{-\varphi^2/2\sigma^{-1}}$, σ plays the role of the inverse variance (higher σ values shrink the vision cone).

The model is thus fully controlled by two non-dimensional parameters: the *reduced temperature* $T \equiv T/J$, and the *non-reciprocal parameter* $\sigma \geq 0$ quantifying the departure from the reciprocal $2dXY$ model. Time is expressed in units of γ/J . Importantly, as $g_\sigma(\varphi_{ij})$ depends on θ_i but not θ_j , Eq.(1) cannot be thought of as an equilibrium dynamics driven by a Hamiltonian-like function $\mathcal{H} = -J \sum g_\sigma(\varphi_{ij}) \mathbf{S}_i \cdot \mathbf{S}_j$. Indeed, in the presence of NR interactions the energy of a bond is ambiguous, as $g_\sigma(\varphi_{ij}) \neq g_\sigma(\varphi_{ji})$. Generally speaking, the defining feature of a NR system is its dynamics, that here we chose to be of the (noisy) Kuramoto-type [15, 37] (contrary to Glauber type as considered in [48]). Thus, σ breaks *parity*, $O(2)$ *rotational* and *time-reversal* symmetry [53, 54] (see SM[52]).

Topological defects in the $2dXY$ model are point-like and have integer winding numbers, or charges, q [4]. A defect of charge q is identified in the dual lattice as a plaquette around which the circulation of the phase field (the sum of the phase differences) is $\sum \Delta\theta_{ij} = 2\pi q$. The field disturbance they generate, in the spin-wave approximation, reads $\theta(x, y) = q \text{atan}(y/x) + \mu$, where the integration constant μ physically represents its *shape* (see Fig.1(b-e)). Building on this reference form, we define, in our non-reciprocal model, the (scalar) shape of a defect as $\mu = \text{Arg}(\sum_{j=1}^3 e^{i[\theta_j - q \text{atan}(y_j/x_j)])})$, where the sum runs over the sites defining the plaquette in which the defect lies. In systems with $O(2)$ symmetry, $q = \pm 1$ defects are typically referred to as vortices and anti-vortices, regardless of their shape, denoted μ_\pm . As we shall see, for $\sigma \neq 0$, defects’ shape matters: one shall make a distinction between $q = 1$ defects with different values of μ_+ , such as *sources* ($\mu_+ = 0$), *sinks* ($\mu_+ = \pi$) and *vortices* ($\mu_+ = \pm \pi/2$).

Analysing an isolated $q = 1$ defect, one realises that NR interactions *twist* the field around it, *reshaping* all defects besides sources and sinks. A source is marginally stable while sinks are the only stable shapes towards which all the others decay. Figures 2(a-c) show such twisting from an arbitrary initial shape, here $\mu_+ = \pi/4$, towards the sink configuration. In a reciprocal system, the spins around a defect are equally influenced by all their neighbours. In the vicinity of a defect, each spin perceives equal and opposite contributions from its front and back neighbours and its shape is stable. Non-

reciprocal interactions modify this balance. Consider an extreme situation where each spin only “sees” the spin in front. Then spins tend to align with it, as sketched in Fig.2(g), generating a twist of the spin field that reshapes the defect.

To quantify such reshaping, we follow $\mu_+(t)$ in time. As shown in Fig.2(i), for $\sigma = 0$, the shape of the defect remains, as expected, unchanged. For any $\sigma > 0$, μ_+ spontaneously decays to π (sink), from any initial value μ_0 (here $\mu_0 = 1, 5$). Although σ appears to control the decay rate, those curves do not collapse when plotted against σt : σ^{-1} does not define a characteristic timescale. To gain some insight, we derive (in [52]) the following continuous approximation of Eq.(1) in a square lattice at $T = 0$ for small σ :

$$\frac{\dot{\theta}(x, y)}{2} = \cos \theta_x \sin \theta_{xx} + \cos \theta_y \sin \theta_{yy} + \sigma (\cos \theta \sin \theta_x \cos \theta_{xx} + \sin \theta \sin \theta_y \cos \theta_{yy}) \quad (2)$$

where $\theta_a = \frac{\partial \theta}{\partial a}$ and $\theta_{aa} = \frac{1}{2} \frac{\partial^2 \theta}{\partial a^2}$. From this expression, it is now clear that (i) σ cannot be absorbed in the time unit (ii) the dynamics is μ -invariant if and only if $\sigma = 0$. Focusing now on small gradients, one can describe the dynamics in the continuum as

$$\dot{\theta} = \Delta \theta + 2\sigma (\nabla \times \mathbf{S})_z \equiv f_{\text{EL}}(\mu_+, \mu_0) + \sigma f_{\text{NR}}(\mu_+) \quad (3)$$

where Δ is the Laplacian operator and \mathbf{S} the spin vector field. The reciprocal part of the kernel is responsible for the elastic force f_{EL} (the $2dXY$ model in the spin wave approximation [5]) while the NR part gives rise to a novel twisting term f_{NR} , given by the vorticity of the spin field. The latter directly stems from the head-tail asymmetry in the influence of the neighbourhood on a spin. This rotational nature of f_{NR} powers the twist from the inside of the defect’s core; the elastic term distributes the stress isotropically, explaining why the twist first takes place close to the defect core before radially propagating outwards, see Fig.2(b). As for $\mu_+ = 0, \pi$, $f_{\text{NR}} = 0$, sources and sinks are fixed points. Sinks are attractors of the dynamics, while sources are only marginally stable at $T = 0$ – thermal noise induces fluctuations in the field, generating a non-vanishing f_{NR} . Figure 2(j) shows how any initial shape μ_0 flows towards $\mu_+ = \pi$. While f_{NR} only depends on the current configuration, f_{EL} retains memory of the original defect configuration μ_0 , trying to restore it against f_{NR} . As shown in the inset of Fig.2(j), for small enough σ and μ_0 , f_{EL} can balance f_{NR} such that μ_+ never reaches $\mu_+ = \pi$.

We now turn our attention on $q = -1$ defects. Non-reciprocal forces polarise the field around isolated $q = -1$ defects, following the mechanism depicted in Fig.2(h), creating two regions pointing in opposite directions and separated by a growing *polarisation axis*, leading to the final state of Fig.2(f). Importantly, the polarised field

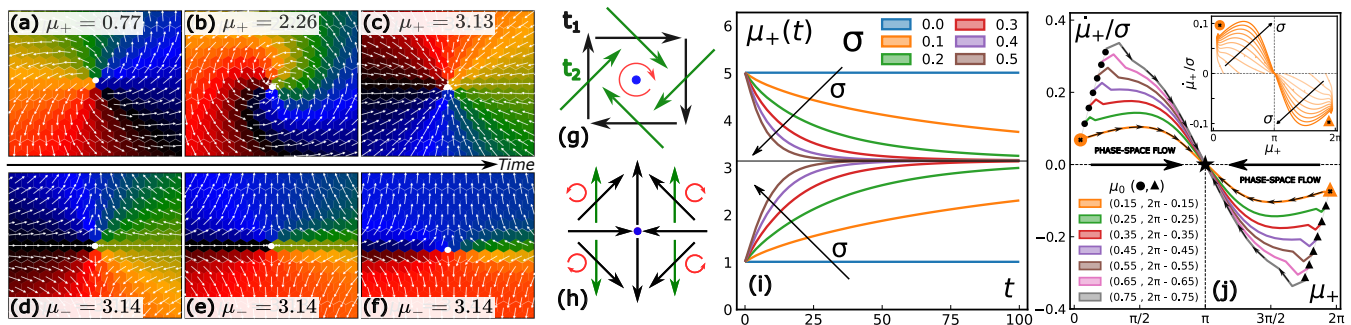


FIG. 2. (a,b,c) Twist of a positive defect towards the sink state ($\mu_+ = \pi$). Same color code as in Fig.1. (d,e,f) Polarisation of a negative defect, leaving $\mu_- = \pi$ unchanged. (g,h) Sketches of the reshaping mechanism for a positive and negative defect, in black at time t_1 and in green at time $t_2 > t_1$. (i) Evolution a $q = +1$ defect's shape for different values of σ from two different initial configurations. The horizontal line corresponds to $\mu_+ = \pi$. (j) Phase space plot $\mu_+ - \mu_+/\sigma$ of a twisting defect at $\sigma = 0.5$. They all flow towards the central star, the stable sink state. Inset: same flow plot for two initial shapes $\mu_0 = 0.15$ and $\mu_0 = 2\pi - 0.15$, now for different values of $\sigma = 0.1\dots 0.5$. $T = 0$ for all panels.

around a $q = -1$ defect is now locally translational invariant: it provides a preferred path for defect motion, as it only takes a few spins flips to slide along the axis. On the contrary, it is very unfavourable for the defect to move perpendicularly to the axis as it would require a macroscopic number of spin flips. Obviously, the local field is no longer isotropic but remains centrally symmetric with respect to the defect core, explaining why $\mu_-(t)$ is constant over the polarisation process, see Fig.2(d-f).

At equilibrium, twisted defects relax towards the non-twisted ones (from (b) to (a) in Fig.2) under the action of f_{EL} . Defects in nematic liquid crystals can also relax to specific shapes μ if the bend and splay constants are different [11]. However, while those behaviours are purely relaxational and therefore decrease the stresses on the system over time, the dynamics reported in here is essentially different as NR interactions induce such twists spontaneously from isotropic isolated defect configurations.

As NR interactions reshape defects, they strongly impact their annihilation dynamics. In the reciprocal $2dXY$ model, defects of opposite charge $\pm q$ at a distance R attract each other with a Coulomb force $F \sim q^2/R$ that drives their annihilation at low $T < T_{KT} = 1.42$ [5, 9, 15, 16, 52]. The model is symmetric under parity and thus $\pm q$ defects are equivalent. NR interactions break such symmetry, can *enhance* or *hinder* the annihilation process and induce effective *transverse forces*, depending on the specific shape of the defects involved.

To grasp the annihilation process, we manually create a pair of defects of charge $q = \pm 1$ and initial shapes μ_{\pm} at a distance R_0 , imposing periodic boundary conditions. To obtain a non-twisted initial configuration, we impose the *least distortion condition* $\mu_- - \mu_+ = \pi$ (derived in the SM [52]). We then let the system evolve at $T = 0.08 T_{KT}$ and track defects over time to obtain their displacement $d_{\pm}(t)$ and their mutual distance $R(t)$.

We focus first on two limit situations, involving sources and sinks, that will provide our reference scenarios, to then move to the description of more general annihilation process, as illustrated in Fig.3(a-c).

A source, $\mu_+ = 0$, can only be initially paired with a $\mu_- = \pi$ defect that grows a polarisation axis along the core-to-core direction, see Fig.3(a). Such polarisation provides a preferential annihilation pathway. As shown in Fig.3(d), $R(t)$ decays faster for larger values of σ , which translates into a reduced annihilation time τ (that appears to be independent of T , see Fig.3(e)). Moreover, and in contrast with the $2dXY$ model, $q = \pm 1$ defects are no longer equivalent: $+1$ defects move faster than -1 defects in the enhanced annihilation process (Fig.3(f)).

For a sink, $\mu_+ = \pi$, the polarisation axis of the -1 defect, $\mu_- = 0$, grows perpendicularly to the core-to-core direction, as illustrated in Fig.3(b). Such structure pins the -1 defect along the axis, hindering its annihilation with the $+1$ defect. As the formation rate of the polarisation axis increases linearly with σ (see [52]), $R(t)$ exhibits a slower decay (solid lines in Fig.3(d)) and the annihilation is dramatically slowed down (up to a factor 10^2 with respect to the $2dXY$ case, see Fig.3(e)).

For any other initial pair, the $+1$ defect experiences a twist due to a non-vanishing f_{NR} . On the other hand, the -1 defect grows an oblique polarisation axis, that eventually twists close to the $+1$ defect core, see Fig. 3(c). Then, once such preferential road has been created, the -1 moves along it until the polarisation axis becomes perpendicular to the $+1/-1$ direction.

Such annihilation processes are summarised by the map of the annihilation time τ (normalised by τ_{XY} , the corresponding time in the $2dXY$ model) in the $\mu_+-\sigma$ plane shown in Fig.3(g). Annihilation times are much smaller than in the reciprocal case for small μ_+ and large σ (blue region in Fig.3(g)); and much larger for $\mu_+ \approx \pi$ (red region). Between the two extreme cases, the competition

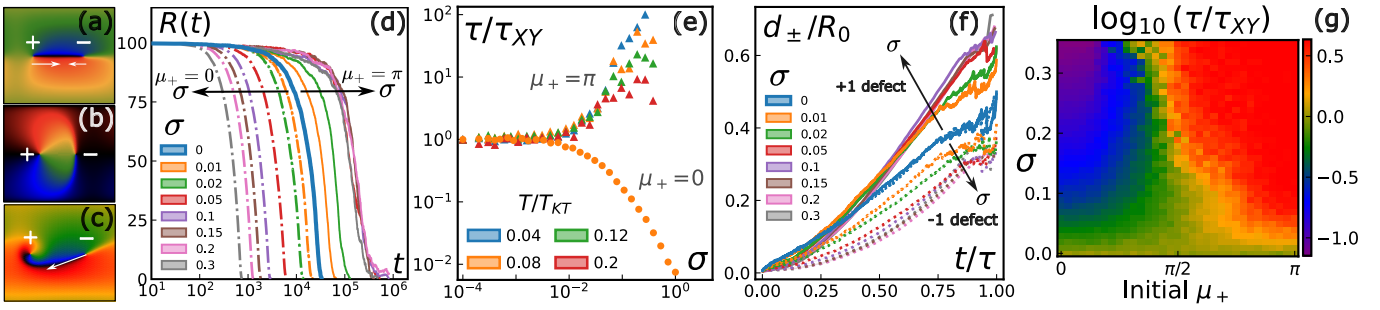


FIG. 3. (a,b,c) Configurations of two defects of opposite charge at $T = 0, \sigma = 0.35$ with $\mu_+ = 0, \pi, \pi/2$, respectively. Arrows indicate their displacement. (d) Inter-defect distance $R(t)$ between a $\mu_+ = 0$ and a $\mu_- = \pi$ (dashed lines) and a $\mu_+ = \pi$ and a $\mu_- = 0$ (solid lines) pair. In both cases, $T = 0.08 T_{KT}, L = 2R_0 = 200$. Sources enhance annihilation while sinks hinder it. (e) Annihilation time τ corresponding to the two previous cases ($\mu_+ = 0, \pi$), rescaled by the one in the $2dXY$ case, for different temperatures (using $L = 2R_0 = 100$). For $\mu_+ = 0$, we only display the case $T = 0.08 T_{KT}$ as curves for different temperatures superimpose. (f) Distance travelled d_{\pm}/R_0 by +1 (solid lines) and -1 (dotted lines) defects in the configuration shown in panel (a) ($\mu_+ = 0, \mu_- = \pi$) for several values of σ . (g) Colour map of the annihilation time in log-scale in terms of different initial shapes $0 \leq \mu_+ \leq \pi$ and values of σ (using $L = 64, R_0 = 30$ and $T = 0.08 T_{KT}$).

between f_{NR} and f_{EL} can smoothly tune the annihilation time to make it longer or shorter than in the classical picture.

As NR interactions impact significantly the defect annihilation, it is worth exploring its consequences in the coarsening dynamics of the system. We thus analyse the relaxation following a quench from a disordered state, with a large number of defects, to very low temperatures, where only a few bonded defects might persist [10, 16, 55]. We show in Fig.4(a) a snapshot of the system during its relaxation at $T = 0$ and in Fig.4(b) the time evolution of the defect density for different values of σ at $T/T_{KT} = 0.08$. Occasionally, defect pairs spontaneously generate to temporarily release local excessive forces, but the newly created defects rapidly annihilate (cf. [52] Movie 6b). As such, we find that the steady state is typically defectless at such low temperatures. However, the coarsening gets significantly slower for larger values of σ : +1 defects quickly decay to sinks, giving

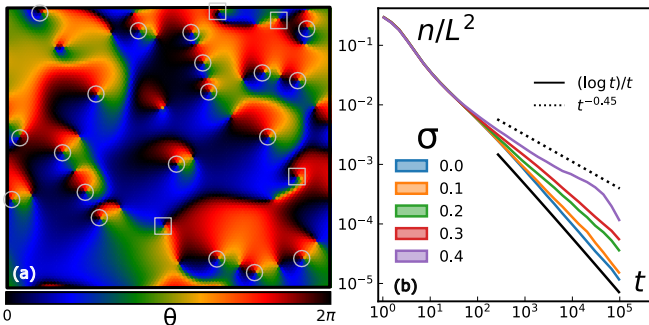


FIG. 4. (a) Snapshot of a $L = 100$ system at $t = 200$ with $T = 0, \sigma = 0.3$. Sink defects ($q = +1, \mu_+ = \pi$) are circled. The other $q = +1$ defects are squared (negative defects are not highlighted). (b) Time evolution of the defect density n/L^2 , for $L = 200, T = 0.08 T_{KT}$ and different σ .

rise to *chains of sinks* (circles in Fig.4(a)) separated by -1 defects with polarisation axes perpendicular to the +1/-1 direction. Those large-scale structures are long lived, providing an explanation of the slowing down of the decay of the numbers of defects in time. It is worth noting though that such structures might also trigger abrupt relaxation events, where the annihilation of one pair of defects triggers the annihilation of all the other defects along the chain. In the $2dXY$ model, those structures are highly unstable and thus never observed.

To conclude, we have shown how NR interactions reshape topological defects in a paradigmatic continuous spin system. In short, non-reciprocity twists the phase field, breaking the parity and rotational symmetry of the $2dXY$ model. In the regime of small deviations from homogeneity, non-reciprocity translates into a novel term in the continuum dynamical equation of the spin field, proportional to its vorticity. The impact of this new term is to segregate defects according to their specific phase, or shape (on top of their charge), leading to a rich phenomenology for pair annihilation. The latter can dramatically speed up or slow down, depending on the specific phase field between defects, resulting from the combination of the non-reciprocal twist and the generalised elasticity of the system. Such intricate scenario goes well beyond the isotropic annihilation of defects in the $2dXY$ model, driven by an effective Coulomb interaction. While we cannot definitively rule out the possibility of describing these intricate dynamics more concisely and uniformly through an effective, anisotropic interaction between defects, in the spirit of Kosterlitz and Thouless theory, the scenario we have outlined appears to be more complex than what would result from simple pairwise interactions. The present study of non-reciprocal defects opens new venues for the dynamical control of topological charges in non-equilibrium systems.

Acknowledgements D.L. and I.P. acknowledge DURSI for financial support under Project No. 2021SGR-673. I.P. and Y.R. acknowledge support from Ministerio de Ciencia, Innovación y Universidades MCIU/AEI/FEDER for financial support under grant agreement PID2021-126570NB-100 AEI/FEDER-EU. D.L. acknowledges MCIU/AEI for financial support under grant agreement PID2022-140407NB-C22. I.P. acknowledges Generalitat de Catalunya for financial support under Program Icrea Acadèmia. Y.R. thanks Elisabeth Agoritsas and Boris Bergsma for fruitful discussions.

* rouzaire.ylann@gmail.com

- [1] V. L. Berezinskii, *Sov. Phys. JETP* **32**, 493 (1971).
- [2] J. M. Kosterlitz and D. J. Thouless, *J. Phys. C* **6**, 1181 (1973).
- [3] J. M. Kosterlitz, *J. Phys. C* **7**, 1046 (1974).
- [4] N. D. Mermin, *Rev. Mod. Phys.* **51**, 591 (1979).
- [5] P. M. Chaikin, T. C. Lubensky, and T. A. Witten, Vol. 10 (Cambridge University Press, 1995).
- [6] D. R. Nelson, (Cambridge University Press, 2002).
- [7] T. W. Kibble, *J. Phys. A: Math. Gen.* **9**, 1387 (1976).
- [8] W. H. Zurek, *Nature* **317**, 505 (1985).
- [9] B. Yurke, A. Pargellis, T. Kovacs, and D. Huse, *Phys. Rev. E* **47**, 1525 (1993).
- [10] A. Jelic and L. Cugliandolo, *J. Stat. Mech. Theory Exp.* **2011** (2011).
- [11] D. J. G. Pearce and K. Kruse, *Soft Matter* **17**, 7408 (2021).
- [12] L. Giomi, M. J. Bowick, P. Mishra, R. Sknepnek, and M. C. Marchetti, *Philos. Trans. Royal Soc. A* **372**, 20130365 (2014).
- [13] D. Pearce, S. Gat, G. Livne, A. Bernheim-Groswasser, and K. Kruse, *arXiv preprint arXiv:2010.13141* (2020).
- [14] L. Braverman, C. Scheibner, B. VanSaders, and V. Vitelli, *Phys. Rev. Lett.* **127**, 268001 (2021).
- [15] Y. Rouzaire and D. Levis, *Phys. Rev. Lett.* **127** (2021).
- [16] Y. Rouzaire and D. Levis, *Front. Phys.* **10**, 785 (2022).
- [17] S. Shankar, A. Souslov, M. J. Bowick, M. C. Marchetti, and V. Vitelli, *Nat. Rev. Phys.* **4**, 380 (2022).
- [18] E. S. Bililign, F. Balboa Usabiaga, Y. A. Ganan, A. Poncet, V. Soni, S. Magkiriadou, M. J. Shelley, D. Bartolo, and W. T. Irvine, *Nat. Phys.* **18**, 212 (2022).
- [19] A. Chardac, L. A. Hoffmann, Y. Poupard, L. Giomi, and D. Bartolo, *Phys. Rev. X* **11**, 031069 (2021).
- [20] A. Poncet and D. Bartolo, *Phys. Rev. Lett.* **128**, 048002 (2022).
- [21] T. B. Saw, A. Doostmohammadi, V. Nier, L. Kocgozlu, S. Thampi, Y. Toyama, P. Marcq, C. T. Lim, J. M. Yeomans, and B. Ladoux, *Nature* **544**, 212 (2017).
- [22] K. Kawaguchi, R. Kageyama, and M. Sano, *Nature* **545**, 327 (2017).
- [23] K. Copenhagen, R. Alert, N. S. Wingreen, and J. W. Shaevitz, *Nat. Phys.* **17**, 211 (2021).
- [24] Y. Maroudas-Sacks, L. Garion, L. Shani-Zerbib, A. Livshits, E. Braun, and K. Keren, *Nat. Phys.* **17**, 251 (2021).
- [25] P. Digregorio, D. Levis, L. F. Cugliandolo, G. Gonnella, and I. Pagonabarraga, *Soft Matter* **18**, 566 (2022).
- [26] S. Shankar, S. Ramaswamy, M. C. Marchetti, and M. J. Bowick, *Phys. Rev. Lett.* **121**, 108002 (2018).
- [27] D. Pearce, J. Nambisan, P. Ellis, A. Fernandez-Nieves, and L. Giomi, *Phys. Rev. Lett.* **127**, 197801 (2021).
- [28] X.-q. Shi, F. Cheng, and H. Chaté, *Phys. Rev. Lett.* **131**, 108301 (2023).
- [29] J. Agudo-Canalejo and R. Golestanian, *Phys. Rev. Lett.* **123**, 018101 (2019).
- [30] P. A. Abrams, *Annu. Rev. Ecol. Evol. Syst.* **31**, 79 (2000).
- [31] I. D. Couzin, J. Krause, N. R. Franks, and S. A. Levin, *Nature* **433**, 513 (2005).
- [32] C. Castellano, S. Fortunato, and V. Loreto, *Rev. Mod. Phys.* **81**, 591 (2009).
- [33] R. Pastor-Satorras, C. Castellano, P. Van Mieghem, and A. Vespignani, *Rev. Mod. Phys.* **87**, 925 (2015).
- [34] V. Ros, F. Roy, G. Biroli, G. Bunin, and A. M. Turner, *Phys. Rev. Lett.* **130**, 257401 (2023).
- [35] J. Grauer, F. Schmidt, J. Pineda, B. Midtvedt, H. Löwen, G. Volpe, and B. Liebchen, *Nat. Comm.* **12**, 6005 (2021).
- [36] M. Rubenstein, A. Cornejo, and R. Nagpal, *Science* **345**, 795 (2014).
- [37] M. Fruchart, R. Hanai, P. B. Littlewood, and V. Vitelli, *Nature* **592**, 363 (2021).
- [38] D. March, J. Múgica, E. E. Ferrero, and M. C. Miguel, *arXiv preprint arXiv:2310.15592* (2023).
- [39] A. Ivlev, J. Bartnick, M. Heinen, C.-R. Du, V. Nosenko, and H. Löwen, *Phys. Rev. X* **5**, 011035 (2015).
- [40] L. P. Dadhichi, J. Kethapelli, R. Chajwa, S. Ramaswamy, and A. Maitra, *Phys. Rev. E* **101**, 052601 (2020).
- [41] Z. You, A. Baskaran, and M. C. Marchetti, *Proc. Natl. Acad. Sci.* **117**, 19767 (2020).
- [42] S. Saha, J. Agudo-Canalejo, and R. Golestanian, *Phys. Rev. X* **10**, 041009 (2020).
- [43] M. Han, M. Fruchart, C. Scheibner, S. Vaikuntanathan, J. J. De Pablo, and V. Vitelli, *Nat. Phys.* **17**, 1260 (2021).
- [44] Y. Avni, M. Fruchart, D. Martin, D. Seara, and V. Vitelli, *arXiv preprint arXiv:2311.05471* (2023).
- [45] A. Benois, M. Jardat, V. Dahirel, V. Démery, J. Agudo-Canalejo, R. Golestanian, and P. Illien, *Phys. Rev. E* **108**, 054606 (2023).
- [46] N. Rana and R. Golestanian, *arXiv preprint arXiv:2306.03513* (2023).
- [47] D. J. Hickey, R. Golestanian, and A. Vilfan, *arXiv preprint arXiv:2305.01077* (2023).
- [48] S. A. Loos, S. H. Klapp, and T. Martynec, *Phys. Rev. Lett.* **130**, 198301 (2023).
- [49] D. S. Seara, A. Piya, and A. P. Tabatabai, *J. Stat. Mech. Theory Exp.* **2023**, 043209 (2023).
- [50] Q.-s. Chen, A. Patelli, H. Chaté, Y.-q. Ma, and X.-q. Shi, *Phys. Rev. E* **96**, 020601 (2017).
- [51] K. V. Mardia, P. E. Jupp, and K. Mardia, Vol. 2 (Wiley Online Library, 2000).
- [52] See Supplemental Material at doi:....
- [53] S. A. M. Loos and S. H. L. Klapp, *New J. Phys.* **22**, 123051 (2020).
- [54] T. Suchanek, K. Kroy, and S. A. Loos, *arXiv preprint arXiv:2305.05633* (2023).
- [55] F. Rojas and A. Rutenberg, *Phys. Rev. E* **60**, 212 (1999).
- [56] M. Hasenbusch, *J. Phys. A* **38**, 5869 (2005).
- [57] H. Weber and P. Minnhagen, *Phys. Rev. B* **37** (1988).
- [58] P. Butera and M. Comi, *Phys. Rev. B* **50**, 3052 (1994).

Supplementary Movies

We provide short movies to visualize the dynamics at play at the single defect level, at the pair level and finally at the system's level (unidirectional gradient propagation as reported in [48] and coarsening dynamics). All videos can be found on this Youtube channel.

It helps sketching the configuration to understand which spins are mainly influenced by which spins. Here is a correspondence that might help :

Black : $\theta = 0$ (\rightarrow)

Blue : $\theta = \pi/2$ (\uparrow)

Green/yellow : $\theta = \pi$ (\leftarrow)

Red/orange : $\theta = 3\pi/2 = -\pi/2$ (\downarrow)

Single defects

Both movies are at $T = 0, \sigma = 0.3$.

- “1- Twist” :
movie of the twist of a positive defect with an initial shape $\mu_+(t = 0) = 1$. The final state is a sink, easily recognised by the black colour being on the left of the defect.
- “2-Polarisation” :
movie of the twist of a negative defect with an initial shape $\mu_-(t = 0) = 1$.

Pairs of defects

For these videos, the initial separating distance $R_0 = 48$, linear size of the system $L = 100$ lattice spacings. $T = 0$. Hereafter, the reported shapes are understood to be the initial shapes, at $t = 0$.

- “3-XY annihilation” :
Annihilation of a pair. XY equilibrium case : $\sigma = 0$. Note how the θ field conserves its symmetry with respect to the defects cores along the process.
- “4a-enhanced annihilation mu0” :
Enhanced annihilation of a pair $\mu_+ = 0, \mu_- = \pi$ for $\sigma = 0.3$. Note how the θ field loses its equilibrium symmetry along the process. The polarisation axis progressively grows in the direction of the positive defects. Until now, none of the defects move in space. Then the axis reaches the +1 defect. At from this point, both defects run along the axis that now connects them until annihilation.
- “4b-enhanced annihilation mu0.2” :
Enhanced annihilation of a pair $\mu_+ = 0.2, \mu_- = \pi - 0.2$ for $\sigma = 0.3$. Here the initial shape of the positive defect $\mu_+ = 0.2 \neq 0$ so the positive defect should, if it were isolated, decay to the sink state. It does indeed start to twist in the first instants of the movie but the negative defect rapidly polarises its surroundings: the polarisation axis reaches the

positive defect before it actually has time to complete its twist. The two defects are now connected by the axis and eventually annihilate following the scenario described above for a pure source $\mu_+ = 0$.

- “5a-hindered annihilation mu pi” :
Hindered annihilation of a pair $\mu_+ = \pi, \mu_- = 0$ for $\sigma = 0.3$. Typical configuration where the axis of the negative defect grows perpendicularly, hindering the annihilation process.
- “5b-hindered annihilation mu pi-0.5” :
Hindered annihilation of a pair $\mu_+ = \pi - 0.5, \mu_- = 2\pi - 0.5$ for $\sigma = 0.3$. Since $\mu_- \neq 0, \pi$ the polarisation axis (initially) grows obliquely. Yet, complex dynamics of the surrounding θ field impose an effective force on the axis, such that it becomes perpendicular to the core-to-core direction. Thus, it is hard for the -1 defect to move: the XY annihilation process is hindered.
- “6a-transverse motion mu pi2” :
Transverse motion, for $\mu_+ = \pi/2, \mu_- = 3\pi/2$ and $\sigma = 0.3$. The polarisation axis grows obliquely while the positive defect decays to a sink. The negative defect then follows the polarised path just created. It eventually places itself below the positive defect, because in this configuration the axis is now perpendicular to the core-to-core direction. We are now in a configuration that leads to the hindering of the annihilation process.
- “6b-transverse motion creation defects mu pi2” :
Same initial configuration, but now for $\sigma = 0.5$. Note how the polarisation axis, separating two domains of opposite orientation becomes so thin that the natural elasticity of the θ field cannot support the large gradients $|\nabla\theta|$ at this location. It therefore breaks to relieve the local tension, creating a new pair of defects: the new $+1$ is on the right and meets/annihilate with the old -1 . The new -1 follows the rest of the polarised axis and places itself below the $+1$, for the same reasons as explained above.
- “6c-transverse motion annihilation mu pi2” :
Same initial configuration, but now for $\sigma = 0.2, T = 0.12T_{KT}$. The negative defect first follows the path traced by the axis, then stabilises below the positive defect for the same reasons as explained above. The difference with the two previous videos is that the present one is at finite temperature, such that the thermal fluctuations help the defects to annihilate.

Coarsening dynamics of the system

We provide 3 movies of a $L = 200$ triangular lattice, at $T/T_{KT} = 0.08$.

- “7a-XY system sigma 0” :
XY case: $\sigma = 0$ The field around defects usually is isotropic and non-twisted. Defect annihilate pair by pair following the scenario shown for isolated pairs of defects.
- “7b-NRXY system sigma 0.15” :
Non-reciprocal case: $\sigma = 0.15$. Note how positive defects twist and how negative defects grows their polarisation axes, creating straight lines in the system. Note how the behaviours seen at the level of a single pair of defect are still valid in this many-body system of defects.
- “7c-NRXY system sigma 0.3” :
Non-reciprocal case: $\sigma = 0.3$. Same comments, but the effects are intensified.

Miscellaneous

- “8a-NRXY propagation sigma 0.5” :
Unidirectional propagation of gradients, as already observed by [48].

Implementation details

The code is written in Julia language and is accessible publicly on GitHub at github.com/yrouzaire/NRXY-Model. Visit julialang.org to install Julia.

Equation of motion : adimensionalisation procedure

Under its most general form, the phase of a spin θ_i follows the overdamped Langevin equation

$$\gamma \dot{\theta}_i(t) = J \sum_{j \in \partial_i} g(\varphi_{ij}) \sin(\theta_j - \theta_i) + \sqrt{2k_B T \gamma} \eta_i(t)$$

where J is the elastic constant, γ the damping coefficient, k_B the Boltzmann constant and η a unit gaussian delta correlated noise. Dividing by J leads to

$$\frac{\gamma}{J} \dot{\theta}_i(t) = \sum_{j \in \partial_i} g(\varphi_{ij}) \sin(\theta_j - \theta_i) + \sqrt{\frac{2k_B T \gamma}{J^2}} \eta_i(t).$$

We then normalise time $\tilde{t} = tJ/\gamma$ and define $\tilde{T} = k_B T/J$. One thus obtains

$$\dot{\theta}_i(\tilde{t}) = \sum_{j \in \partial_i} g(\varphi_{ij}) \sin(\theta_j - \theta_i) + \sqrt{\frac{2\tilde{T}\gamma}{J}} \eta_i(\tilde{t}/J)$$

Finally, since the delta function in the variance of the white noise η_i satisfies $\delta(ax) = \frac{\delta(x)}{|a|}$, one obtains the dimensionless equation of motion:

$$\dot{\theta}_i(\tilde{t}) = \sum_{j \in \partial_i} g(\varphi_{ij}) \sin(\theta_j - \theta_i) + \sqrt{2\tilde{T}} \eta_i(\tilde{t}).$$

We numerically integrate this equation in time using the Euler-Maruyama update rule:

$$\theta_i(t+dt) = \theta_i(t) + dt \sum_{j \in \partial_i} g(\varphi_{ij}) \sin(\theta_j - \theta_i) + \sqrt{2dt \cdot \tilde{T}} \eta_i$$

where the timestep $dt = 0.1/z$, where z is the coordination number (the number of nearest neighbours) and $\eta_i \sim \mathcal{N}(0, 1)$.

Symmetries of the system

The equilibrium XY model is invariant under global rotation of the spins $\{\theta\} \rightarrow \{\theta + \alpha\}$ because the alignment term between two spins i and j only depends on the difference of the spins orientation:

$$\sin((\theta_j + \alpha) - (\theta_i + \alpha)) = \sin(\theta_j - \theta_i) \quad (4)$$

The reciprocal XY model is thus invariant under the addition of a global phase – we say it is $O(2)$ invariant or, equivalently, $O(2)$ symmetric– which prevents defects of the same topological charge but of different shapes (different phases) to behave differently.

In our 2D spin system, the parity transformation $\begin{pmatrix} x \\ y \end{pmatrix} \rightarrow \begin{pmatrix} -x \\ y \end{pmatrix}$ can be re-expressed in terms of angles with the transformation $\{\theta\} \rightarrow \{-\theta + \pi\}$. Since the 2dXY model is $O(2)$ symmetric, we only have to check that the equation of motion is invariant under the transformation $\{\theta\} \rightarrow \{-\theta\}$

$$\begin{aligned} \frac{d}{dt}(-\theta_i) &= \sin(-\theta_j - (-\theta_i)) \\ -\frac{d}{dt}(\theta_i) &= -\sin(\theta_j - \theta_i) \\ \frac{d}{dt}(\theta_i) &= \sin(\theta_j - \theta_i) \\ \dot{\theta}_i &= \sin(\theta_j - \theta_i) \end{aligned} \quad (5)$$

So the XY model is indeed invariant under parity. Note that the parity transformation transforms a $q = +1$ defect into a $q = -1$ and vice-versa, such that XY defects behave in the same fashion regardless of their charge.

On the other hand, the non-reciprocal kernel g violates all the previous symmetries. Indeed, while the alignment term depends on the difference of the spins orientation $\theta_j - \theta_i$, g only depends on the orientation of the spin i . Therefore, $g(\theta) \neq g(\theta + \alpha)$ and the system is no longer $O(2)$ invariant. This is consistent with the results of the main text, where different shapes of the same topological charge (sinks and sources for $+1$ defects for example) behave in a totally different fashion. In the same spirit, $g(\theta) \neq g(-\theta)$, which prevents the system from satisfying parity. This is consistent with the difference in the dynamics between ± 1 defects in the non-reciprocal case.

For instance, in the enhanced annihilation mechanism, positive defects move faster than negative defects, see Fig.3f of the main text.

Both claims are true for all kernels that do not depend on $\theta_j - \theta_i$ but instead only depend on θ_i .

Numerical Implementation of the Square and Triangular Lattices

All the values of θ_i are stored in a square matrix for numerical efficiency, even for the triangular lattice. The topology of the network is encoded in the definition of the nearest neighbours, as shown in Fig.5. The indices $i = 1, \dots, L$ correspond to the rows and run from top to bottom. The indices $j = 1, \dots, L$ correspond to the columns and run from left to right.

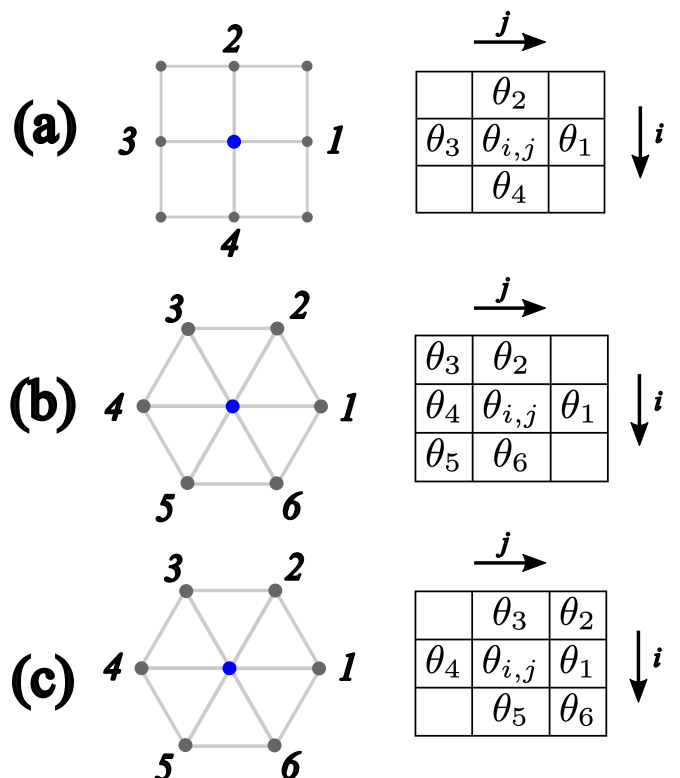


FIG. 5. Nearest neighbours structure for

(a) square lattice, for all i, j .

(b) triangular lattice, for i even and all j .

(c) triangular lattice, for i odd and all j .

A triangular lattice can be thought as a square lattice with all odd rows laterally displaced by one half of the lattice spacing.

Computation of the spatial correlation function

We define the spatial correlation functions

$$C(r) = \langle \mathbf{S}_i \cdot \mathbf{S}_j \rangle = \langle \cos(\theta_i - \theta_j) \rangle \quad (6)$$

where spins i and j are separated by a euclidian distance r . The brackets $\langle \cdot \rangle$ denote an ensemble average over thermal realisations (or equivalently, over all spins). Computing directly such a quantity in a $L \times L$ system scales as $\mathcal{O}(L^3)$, which is prohibitive for large systems. For numerical efficiency, we compute it in the Fourier space, which reduces the numerical cost to $\mathcal{O}(L^2 \log L)$. First note that, by trigonometric identities,

$$\cos(\theta_i - \theta_j) = \cos(\theta_i) \cos(\theta_j) + \sin(\theta_i) \sin(\theta_j) \quad (7)$$

The term $\cos(\theta_i) \cos(\theta_j)$ is a convolution and can be easily handled in Fourier space.

We note the Fourier transform operator \mathcal{F} and its inverse \mathcal{F}^{-1} . We note “ \cdot^2 ” the element-wise square operator: if x is a vector of components x_i , then $x \cdot^2$ is a vector of the same length of components $(x_i)^2$.

With this notation in mind, the $2d$ spatial correlation function can be expressed as

$$C_{2d} = C(r_x, r_y) = |\mathcal{F}^{-1}(|(\mathcal{F}[\cos \theta]) \cdot^2 + (\mathcal{F}[\sin \theta]) \cdot^2|)| \quad (8)$$

In a continuum simulation, C_{2d} would be a radial function. Here, because of the discrete nature of the underlying lattice, C_{2d} is slightly anisotropic. To obtain the usual unidimensional $C(r)$, we take the mean of the two principal components (along the axes) and normalise to get $C(r=0) = 1$.

Kosterlitz-Thouless Critical Temperature

As described by Kosterlitz-Thouless theory [2, 3], the $2dXY$ model exhibits a transition from a quasi-ordered phase to a disordered one, due to the unbinding of topological defects, at a temperature denoted T_{KT} .

At high temperatures $T > T_{KT}$, the entropy term wins and single isolated defects become energetically favourable: they proliferate and span the entire system, leading to disorder, characterised by exponentially decaying spatial correlation functions $C(r) \sim e^{-r/\xi}$, where ξ is the correlation length. At low temperatures, the only energetically favourable way for a defect to exist is to be bound with an oppositely charged defect, thus creating a pair. As the perturbation created by bounded defects gets limited to the distance between them, the system can reach quasi-long-range order, characterised by the power-law decay of spatial correlation functions $C(r) \sim r^{-\eta}$. In particular, at the transition temperature $T = T_{KT}$, renormalisation group calculations predict $\eta = 1/4$.

On the square lattice, the value of the critical temperature $T_{KT} = 0.89$ has been deeply investigated [56, 57]. However, the literature is rather scarce regarding the triangular lattice case. Butera and Comi presented in 1994 a high-temperature expansion and concluded $T_{KT} = 1.47$ [58]. Here, we directly measure the spatial correlation function $C(r)$ for different temperatures. The critical

temperature T_{KT} is here determined as the largest temperature for which $C(r)$ is well described by a power-law decay. We present the results in Fig.6(a) for the square lattice and Fig.6(b) for the triangular lattice. For the square lattice, we obtain $T_{KT} = 0.89$, in agreement with the reported values. For the triangular lattice, we obtain $T_{KT} = 1.42$, compatible with the value reported in [58].

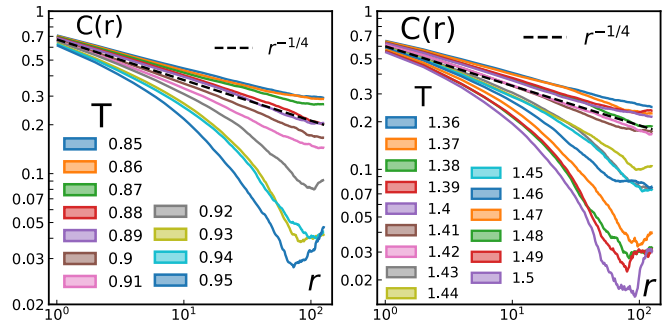


FIG. 6. Spatial correlation function $C(r)$ computed for a $L = 256$ system. **(left)** Square lattice, we obtain $T_{KT} \approx 0.89$ **(right)** Triangular lattice, we obtain $T_{KT} \approx 1.42$.

Let's denote by T_4 (resp. T_6) the critical temperature for the square (resp. triangular) lattice. Interestingly, the ratio $\frac{T_6}{T_4} = \frac{1.42}{0.89} = 1.60 \neq \frac{6}{4}$, meaning that there is more going on than a simple rescaling due to the number of neighbours (as a simple mean-field treatment would predict).

The defects' shape : definition and comments

The field around a topological charge is given by the solution of the $2d$ Poisson equation: $\theta(x, y) = q \arctan(y/x) + \mu$. Once a defect is located, i.e. one knows (x_{core}, y_{core}, q) ; we then naturally define $\mu = \text{Arg} \left\{ \sum_j \exp(i(\theta_j - q u_j)) \right\}$, where the sum runs over the spins surrounding the plaquette of the dual lattice where the defect lies, i is the imaginary unit and Arg is the function that returns the phase of a complex number: $\text{Arg}(re^{i\theta}) = \theta$. Each neighbour j in that sum makes a certain angle $u_j = \arctan(y_j/x_j)$ with respect to the horizontal axis. Irrespective of its position, we note its orientation θ_j . We sketch this in Fig.7, where the red dots are the defects cores. For example, for the square lattice (left panel), $u_j = j\pi/4$, $j = 1, 2, 3, 4$. For the upward (inner) triangular plaquette (central panel), $u_{1,2,3} = \pi/2, -5\pi/6, -\pi/6$. If the defect is located on a downward triangular plaquette (right panel), one has $u_{1,2,3} = 5\pi/6, -\pi/2, \pi/6$.

Note that μ can be thought of as the value of the θ -field at the immediate right side of the defect, as sketched in Fig.8 with the imaginary green arrows.

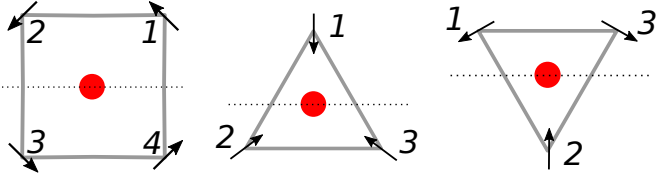


FIG. 7. Defects (red) lie at the centre of the dual plaquettes while the spins live on the lattice nodes (grey). Left panel: the unique plaquette of the square lattice. Centre and right panels: the two plaquettes (resp. up and down) of the triangular lattice. Dotted lines are horizontal and pass through the defects; the angles θ_j and u_j are expressed with respect to that axis in the counterclockwise direction.

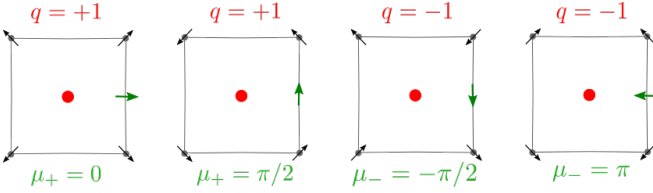


FIG. 8. The defects (red) live at the center of the dual plaquettes. The spins (black) live on the lattice, i.e. on the corners of the plaquette. An easy way to visually identify μ is to imagine the orientation an imaginary spin (green) would have if located at the right edge of the defect ($y = 0$ and thus $\arctan(y/x) = 0$).

Rewriting the equation of motion in terms of first and second spatial derivatives

In this section, we detail the steps to write the equation of motion $\dot{\theta}_i = \sum_j \sin(\theta_j - \theta_i) g(\varphi_{ij})$ in a continuous form, based on derivatives of the field $\theta = \theta(x, y)$, which emphasis the reciprocal and non-reciprocal contributions of the kernel.

Consider a spin i on the square lattice: it has 4 nearest neighbouring spins $j = 1, 2, 3, 4$ (right, top, left, bottom), the orientations of which we note $\theta_{1,2,3,4}$. Those 4 neighbours can be thought to lie on a unit circle centred on the spin i . We call u_j the angle formed by horizontal axis and the location of spin j , see Fig.1a of the main text. In a square lattice, $u_j = \frac{\pi}{2}(j-1)$, $j = 1, \dots, 4$. In a triangular lattice, $u_j = \frac{\pi}{3}(j-1)$, $j = 1, \dots, 6$. Note that u_j and the orientation θ_j are independent.

We start by explaining how *not* to proceed. One could be tempted to identify, from the beginning, $\theta_j - \theta_i$ with the first order derivative of $\frac{\partial \theta}{\partial a}$ ($a = x, y$). The issue is, if one takes the simplest case of the XY model, where the

kernel $g = 1$, one would obtain

$$\begin{aligned} \dot{\theta}_i &= \sum_j \sin(\theta_j - \theta_i) \\ &= \sin\left(\frac{\partial \theta}{\partial x}\right) + \sin\left(\frac{\partial \theta}{\partial y}\right) + \sin\left(-\frac{\partial \theta}{\partial x}\right) + \sin\left(-\frac{\partial \theta}{\partial y}\right) \\ &= 0 \end{aligned} \quad (9)$$

for all fields $\theta(x, y)$ without any assumption. The reason why all terms cancel is that implicitly, one here uses the non-centred numerical definition of derivatives, therefore saying that $\frac{\partial \theta}{\partial x} = \theta_1 - \theta_i = \theta_i - \theta_3$, where the last equality is incorrect in general and especially around a topological defect.

To avoid this problem, one has to go to second order (not surprising if one wants to account for an elastic term) and consider both the spins on the right-left (resp. top-bottom) of the spin i of interest. If one linearises the coupling kernel to first order in σ ($e^{\sigma \cos x} \approx 1 + \sigma \cos x$), one obtains:

$$\begin{aligned} \dot{\theta}_i &= \sum_j \sin(\theta_j - \theta_i) g(\varphi_{ij}) \\ &= \sum_j \sin(\theta_j - \theta_i) [1 + \sigma \cos(\varphi_{ij})] \\ &= \sum_j \sin(\theta_j - \theta_i) [1 + \sigma \cos(\theta_i - u_j)] \\ &= \sum_j \sin(\theta_j - \theta_i) \left[1 + \sigma \cos\left(\theta_i - \frac{\pi}{2}(j-1)\right)\right] \\ &= \sin(\theta_1 - \theta_i) (1 + \sigma \cos \theta_i) \\ &\quad + \sin(\theta_2 - \theta_j) \left[1 + \sigma \cos\left(\theta_i - \frac{\pi}{2}\right)\right] \\ &\quad + \sin(\theta_3 - \theta_i) [1 + \sigma \cos(\theta_i - \pi)] \\ &\quad + \sin(\theta_4 - \theta_i) \left[1 + \sigma \cos\left(\theta_i - \frac{3\pi}{2}\right)\right] \\ &= \sin(\theta_1 - \theta_i) (1 + \sigma \cos \theta_i) \\ &\quad + \sin(\theta_2 - \theta_i) (1 + \sigma \sin \theta_i) \\ &\quad + \sin(\theta_3 - \theta_i) (1 - \sigma \cos \theta_i) \\ &\quad + \sin(\theta_4 - \theta_i) (1 - \sigma \sin \theta_i) \\ &= \sin(\theta_1 - \theta_i) + \sin(\theta_3 - \theta_i) + \sin(\theta_2 - \theta_i) + \sin(\theta_4 - \theta_i) \\ &\quad + \sigma \cos(\theta_i) (\sin(\theta_1 - \theta_i) - \sin(\theta_3 - \theta_i)) \\ &\quad + \sigma \sin(\theta_i) (\sin(\theta_2 - \theta_i) - \sin(\theta_4 - \theta_i)) \end{aligned} \quad (10)$$

One has (the same goes for the vertical direction with θ_2 and θ_4):

$$\begin{aligned} &\sin(\theta_1 - \theta_i) + \sin(\theta_3 - \theta_i) \\ &= 2 \sin\left[\frac{1}{2}(\theta_1 - 2\theta_i + \theta_3)\right] \cos\left[\frac{1}{2}(\theta_1 - \theta_3)\right] \end{aligned} \quad (11)$$

$$\begin{aligned} & \sin(\theta_1 - \theta_1) - \sin(\theta_3 - \theta_1) \\ &= 2 \cos \left[\frac{1}{2} (\theta_1 - 2\theta_i + \theta_3) \right] \sin \left[\frac{1}{2} (\theta_1 - \theta_3) \right] \end{aligned} \quad (12)$$

Now if, one identifies the differences as

$$\begin{aligned} \frac{\partial \theta}{\partial x} &= \frac{\theta_1 - \theta_3}{2} \\ \frac{\partial \theta}{\partial y} &= \frac{\theta_2 - \theta_4}{2} \\ \frac{\partial^2 \theta}{\partial x^2} &= \theta_1 - 2\theta_i + \theta_3 \\ \frac{\partial^2 \theta}{\partial y^2} &= \theta_2 - 2\theta_i + \theta_4 \end{aligned} \quad (13)$$

one then obtains the result of the main text Eq. (2):

$$\begin{aligned} \frac{\dot{\theta}}{2} &= \cos \theta_x \sin \theta_{xx} + \cos \theta_y \sin \theta_{yy} \\ &+ \sigma (\cos \theta \sin \theta_x \cos \theta_{xx} + \sin \theta \sin \theta_y \cos \theta_{yy}) \end{aligned} \quad (14)$$

where $\theta = \theta(x, y)$, $\theta_a = \frac{\partial \theta}{\partial a}$ and $\theta_{aa} = \frac{1}{2} \frac{\partial^2 \theta}{\partial a^2}$, $a = x, y$.

In this small gradients limit, one can approximate $\cos \alpha \approx 1$ and $\sin \alpha \approx \alpha$. One thus obtains

$$\frac{\dot{\theta}}{2} = \theta_{xx} + \theta_{yy} + \sigma (\cos(\theta) \cdot \theta_x + \sin(\theta) \cdot \theta_y) \quad (15)$$

The first two terms give the Laplacian operator that physically represents the elasticity of the θ field. The last two terms can be rewritten as follows:

$$\cos(\theta) \cdot \theta_x + \sin(\theta) \cdot \theta_y = \partial_x (\sin \theta) - \partial_y (\cos \theta) = (\nabla \times \mathbf{S})_z \quad (16)$$

where $\mathbf{S} = (\cos \theta, \sin \theta)$ is the spin vector field.

Constructing a pair of defects with controlled shapes

The first step to investigate an isolated pair of defects is to be able to create 2 defects with controlled shapes μ_+ and μ_- . To do so, recall that around an ideal topologi-

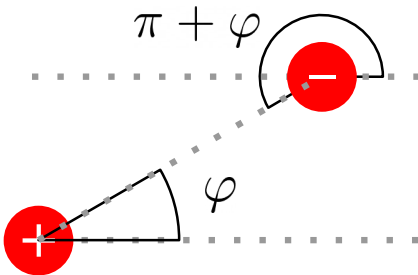


FIG. 9. Sketch of a pair of defects and definition of the polar angle φ that the negative defect makes with respect to the positive defect.

cal defect, $\theta = q \arctan(y/x) + \mu$. In polar coordinates,

where $\varphi = \arctan(y/x)$ (depicted in Fig.9), the field contribution from the defect reads $\theta = q\varphi + \mu$.

It follows that if one creates a positive defect with μ_1 and a negative defect with μ_2 , both fields will add up. At the location of the negative defect, the sum of the two contributions is

$$\mu_- = [\mu_1 + (+1)\varphi] + [\mu_2] = \mu_1 + \mu_2 + \varphi. \quad (17)$$

At the location of the positive defect, the sum of the two contributions is

$$\mu_+ = [\mu_1] + [(-1)(\varphi + \pi) + \mu_2] = \mu_1 + \mu_2 - \pi - \varphi. \quad (18)$$

Those are the concrete equations we use to create defects with controlled μ_+, μ_-, φ (only 2 of these 3 parameters are independent), tuning $\mu_1 + \mu_2$ to obtain the desired μ_+, μ_- .

Also, one can get rid of the artificial μ_1, μ_2 by combining these equations to obtain:

$$\mu_- - \mu_+ = \pi + 2\varphi. \quad (19)$$

As it creates the smoothest possible field, this equation represents the state of least distortion. It also highlights that only two of these three parameters are independent. In the main text, and without loss of generality, we work with $\varphi = 0$: the defects are horizontally aligned and the positive defect is on the left side.

Growth of the polarisation axis with σ

Non-reciprocal interactions create large scale collective structures such as the polarisation axis of the $q = -1$ defects. The larger σ , the more influenced spins are by the neighbours they look at. This favouring large coherent structures and the growth of the polarisation axis is faster for larger σ .

To quantify such process, one indirect but simple and informative measure is to monitor the *nematic* order parameter $Q = \frac{1}{N} \sum_j e^{2i\theta_j}$. We show in Fig.10 the time evolution of Q for a system composed of a single negative defect (centered). The initial condition is a perfectly isotropic defect $\theta(x, y) = -\text{atan}(y/x) + \mu_-$, $Q(t=0) = 0$, $P(t=0) = 0$. With time, the polarisation axis extends, separating two regions in which the *polar* order P increases (spins synchronise). Yet, those two regions have opposite orientation, so the global P remains zero throughout the process. However, the nematic order parameter Q increases as the contributions from the two regions add up. The left panel of Fig.10 shows that the larger the non-reciprocal parameter σ , the faster the dynamics. The right panel of Fig.10 shows the same data but as a function of σt (in a logarithmic scale to emphasis the short time regime). Because the curves collapse at small times, we conclude that σ entirely controls

the small time growth of the axis. However, the long time regime also depends on the elasticity of the θ field, and hence how thin the polarisation axis can be. The larger σ , the thinner the axis can be (because the non-reciprocal forces dominate over the elastic ones), so the system tends to be fully polarised and $Q(t \rightarrow \infty)$ increases.

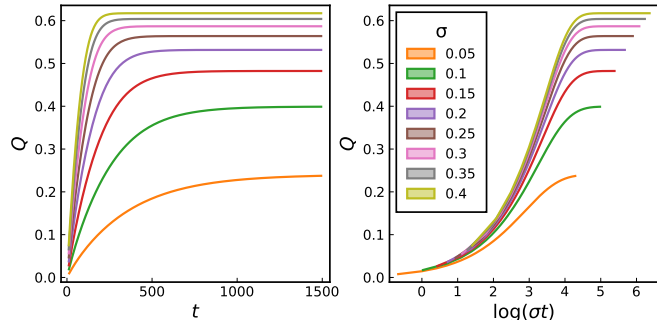


FIG. 10. (left) Nematic order parameter $Q(t)$ of an isolated defect in a 50×50 system at $T = 0$. Different colours correspond to different σ , as indicated in the right panel. (right) Same data, but against $\log(\sigma t)$ instead of t .

Supplementary discussion on the work of Loos, Klapp and Martynec (Phys. Rev. Lett. , 2023)

In their article *Long-Range Order and Directional Defect Propagation in the Nonreciprocal XY Model with Vision Cone Interactions* (2023) [48], Loos, Klapp and Martynec introduced a similar $2dXY$ model with non-reciprocal couplings. In this section, we discuss the differences between both approaches.

Discretisation issues

In [48], a spin j is considered to be in the neighbourhood of a spin i if and only if j is in the vision cone of i . They use a sharp vision cone kernel, as described in orange in Fig.1, such that j is an interacting neighbour of i if and only if the angle between the orientation θ_i of the spin i and the location u_j of the spin j is less than half of the vision cone Θ .

Because the underlying lattice is *discrete*, the sharpness of the kernel induces undesirable artefacts which we illustrate here on a triangular lattice ($z = 6$ is thus the coordination number of the lattice).

The main discretisation effect is the generic change in the number of neighbours as the system evolves in time. This aspect is discussed in depth in [48]. The case $\Theta = 2\pi/z$, $n = 1, \dots, z$, illustrated in Fig.11(a,b), is helpful to understand the issue. If the orientation of a spin i is $\theta_i = \pi/2$, i has 4 neighbours in its vision cone.

If its orientation fluctuates by an infinitesimal amount, it immediately loses one neighbour. The same happens for all values of Θ , as we sketch in Fig. 11(c,d) for an arbitrary vision cone amplitude. The consequence of this brutal change in the number of neighbours is important. If one works with a Monte-Carlo type of dynamics, since the energy is extensive (as opposed to intensive if normalised by the number of contributing neighbours) there exist z regions energetically favourable imposed by the symmetry of the underlying lattice. This strongly promotes a local alignment with the symmetry of the lattice.

If instead one works with a Langevin approach based on extensive (i.e. additive) forces, a similar problem remains. We illustrate in Fig. 11(e) a configuration where the blue spin (in the center) has only one neighbour within its vision cone, while the green spin (on the right) has two neighbours, among which the latter one in blue. The Langevin equation of motion looks like $\dot{\theta}_i = \sum_j \sin(\theta_j - \theta_i) + \sqrt{2T}\nu_i$. For the blue spin, the sum only contains one contribution while for the green spin, it contains 2 terms so it is potentially twice as big. However, the temperature T of the thermal bath is constant. The ratio between the thermal angular diffusion and the interacting force becomes then space and time dependent.

To avoid these issues, one could imagine normalising the energy (or the force in a Langevin-like approach) by the (time-dependent) number of neighbours within the vision cone. However, this introduces another source of non-reciprocity, as the force of green on blue is now twice the force of the blue on green, in absolute value. The introduction of this new source of non-reciprocity has been documented in [59].

These issues are a consequence of having a sharp vision cone kernel. On the contrary, the soft vision cone kernel used in the present work strongly attenuates them. Since the kernel $g(\varphi) = \exp(\sigma \cos(\varphi))$ is continuous and differentiable, a small change in φ can only generate a small change in g . A relevant measure is the sum of the angular weights $\mathcal{G}_i \equiv \sum_{j=1}^z g(\varphi_{ij})$, as it relates to the maximum force a spin can feel. In particular, its dependence on θ_i is related to the discretisation effects; its dependence on σ allows to understand the relative importance of the two terms in the equation of motion: alignment and thermal noise. We have seen above that, in the sharp vision cone case, both a change in orientation θ_i or in the vision cone amplitude Θ , can result in a sudden gain of one neighbour, which translates in a sudden increase (+1) of \mathcal{G}_i . In the soft vision cone case, we want to study the dependence of \mathcal{G}_i on σ and θ_i . To do so, we consider the square lattice for two reasons: (i) the calculations are simpler (ii) discretisation effects in the triangular lattice are less pronounced than for the square lattice; we thus consider the worst case scenario. The sum over the angular weights

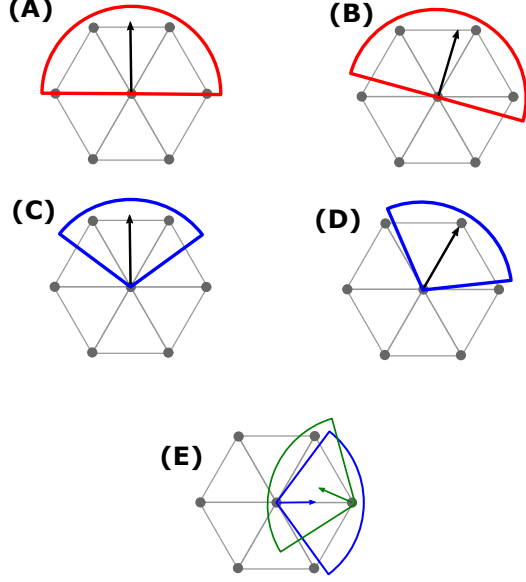


FIG. 11. **(A, B, C, D)** A spin can brutally lose or gain one neighbour within its sharp vision cone during the dynamics. **(E)** The effective temperature felt by two neighbouring spins can be different if their number of neighbours is different.

gives:

$$\begin{aligned}
\mathcal{G}_i &\equiv \sum_{j=1}^4 g(\varphi_{ij}) \\
&= \sum_{j=1}^4 e^{\sigma \cos(\theta_i - u_j)} \\
&= \sum_{j=1}^4 e^{\sigma \cos(\theta_i - (j-1)\frac{\pi}{2})} \\
&= e^{\sigma \cos \theta_i} + e^{\sigma \sin \theta_i} + e^{-\sigma \cos \theta_i} + e^{-\sigma \sin \theta_i} \\
&= 2 \cosh(\sigma \cos \theta_i) + 2 \cosh(\sigma \sin \theta_i)
\end{aligned} \tag{20}$$

Since $|\cos x| \leq 1$ and $|\sin x| \leq 1$, for small σ one can Taylor expand the cosh:

$$\begin{aligned}
\mathcal{G}_i &= 2 + (\sigma \cos \theta_i)^2 + \frac{1}{12} (\sigma \cos \theta_i)^4 + \mathcal{O}(\sigma^6) \\
&+ 2 + (\sigma \sin \theta_i)^2 + \frac{1}{12} (\sigma \sin \theta_i)^4 + \mathcal{O}(\sigma^6) \\
&= 4 + \sigma^2 + \sigma^4 \frac{\cos^4 \theta_i + \sin^4 \theta_i}{12} + \mathcal{O}(\sigma^6)
\end{aligned} \tag{21}$$

We learn that \mathcal{G}_i only varies with the orientation θ_i to *fourth* order in σ . For $\sigma = 0.5$, it implies that $\mathcal{G}_i(\theta)$ varies at most by 0.06 % from its maximum value $\mathcal{G}_i(\theta = n\pi/2)$, $n = 1, \dots, z$ (to be compared to the 100 % of the vision cone model when a spin passes from 1 to 2 neighbours). Indeed, when $\theta = \pi/4$, the mode of the kernel falls in between 2 neighbours, and

$$\begin{aligned}
&\frac{\mathcal{G}_i(\theta = 0; \sigma = 0.5) - \mathcal{G}_i(\theta = \pi/4; \sigma = 0.5)}{\mathcal{G}_i(\theta = 0; \sigma = 0.5)} \\
&= \frac{4.2552 - 4.2526}{4.2552} = 0.0006
\end{aligned} \tag{22}$$

Therefore, the soft vision kernel we propose indeed strongly attenuates the effects stemming from the underlying discrete lattice for the typical range of $\sigma \in [0, 1/2]$ used in this work.

Small vision cones and percolation threshold

Most of the results presented in this work are for values of $\sigma \leq 0.5$. We pushed up to $\sigma = 1$ for Fig.3(e). However, one cannot increase σ up to arbitrarily large values. Indeed, the larger σ gets, the more peaked the kernel $g(x) = \exp(\sigma \cos x)$ becomes. If almost all the mass of the distribution falls between two neighbours, the spin in fact “sees” no neighbour at all, and its dynamics is thus only driven by white noise. In this Letter, we work far from this regime. For instance, for $\sigma = 0.5$, the deviation from an isotropic kernel is moderate: $g(0) = e^{0.5} \approx 1.65$ and the smaller coupling value is $g(\pi) = e^{-0.5} \approx 0.6$, far from negligible. Such pathological limit $\sigma \rightarrow \infty$ is not a specificity of our model. Loos et al. [48], for their sharp vision cone model, report in the same spirit that for vision cones smaller than $\pi/3$ on the triangular lattice ($\pi/2$ on the square lattice), the percolation of the interaction network is no longer guaranteed.

Equation of motion stemming from the XY energy modulated by the kernel

We now compare our Langevin equation of motion to the equation of motion one would obtain from the relaxation driven by an energy function

$$E = - \sum_{i,j} g(\varphi_{ij}) \cos(\theta_j - \theta_i) \tag{23}$$

If $g(x) = \exp(\sigma \cos x)$, the corresponding equations of motions would be ($\Delta\theta_{ij} \equiv \theta_j - \theta_i$ and $\varphi_{ij} \equiv \theta_i - u_j$)

$$\begin{aligned}
\dot{\theta}_i &= -\frac{\partial E}{\partial \theta_i} \\
&= -\sum_j \frac{\partial}{\partial \theta_i} (g(\varphi_{ij}) \cos(\Delta\theta_{ij})) \\
&= \sum_j g(\varphi_{ij}) \sin(\Delta\theta_{ij}) - \cos(\Delta\theta_{ij}) \frac{\partial g(\varphi_{ij})}{\partial \theta_i} \\
&= \sum_j g(\varphi_{ij}) \sin(\Delta\theta_{ij}) + \cos(\Delta\theta_{ij}) (\sigma \sin \varphi_{ij}) \underbrace{\frac{\partial \varphi_{ij}}{\partial \theta_i}}_{=1} g(\varphi_{ij}) \\
&= \sum_j g(\varphi_{ij}) \left[\underbrace{\sin(\Delta\theta_{ij})}_{\text{attraction}} + \underbrace{\sigma \sin(\varphi_{ij}) \cdot \cos(\Delta\theta_{ij})}_{\text{(side) repulsion !}} \right]
\end{aligned} \tag{24}$$

The first term $\sin(\theta_j - \theta_i)$ corresponds to the alignment term in our Langevin description. The additional second term in $\cos(\theta_j - \theta_i)$ favours orthogonal spin configurations, but, due to the $\sin(\varphi_{ij})$ coefficient, this repulsion mainly takes place on the sides of the spin i , “ahead” being in the direction of θ_i . The amplitude of this second term, however, is *a priori* smaller than the first term, since in this work we used $\sigma \leq 1$ and since $|\sin(\varphi_{ij})| \leq 1$. Yet, the impact of this additional term, though only to second order, favours the stabilisation of the sources $\mu_+ \approx 0$, a configuration in which spins are indeed perpendicular.

We report the effect of this additional term on the twist of positive defects in Fig.12. As stated, the $\cos(\theta_j - \theta_i)$ term only has a small amplitude and thus does not change the stable configuration which remains the sink state $\mu_+ = \pi$. However, the decay to this stable state is slower, especially for initial configurations close to sources $\mu_+ = 0 = 2\pi$ (cf. orange or cyan curves). This could have large scale consequences as the sources are the only ones involved in the enhanced annihilation process. If they are slightly stabilised by this repulsive term, the enhanced annihilation process could be even stronger and impact the overall coarsening dynamics.

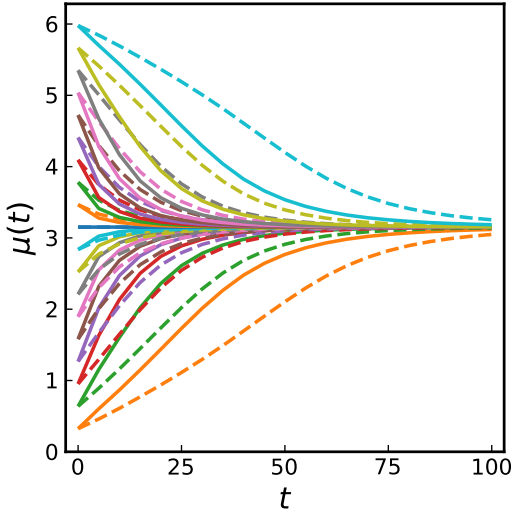


FIG. 12. In the spirit of Fig.2(i) of the main text, we monitor the shape $\mu_+(t)$ of a positive defect over time, for different initial shapes $\mu_+(0)$ (different colours). The solid lines correspond to our Langevin-based model, with only the first alignment term. The dashed lines correspond to equation Eq.(24), with the additional second term.